

Engineering the morphology on layered double hydroxides-induced persulfate activation for enhanced degradation of organic pollutants

Rongyao Wang

University of Jinan

Yanjun Yu

University of Jinan

Ruijuan Zhang

University of Jinan

Xiaohua Ren

University of Jinan

Weilin Guo (✉ chm_guowl@ujn.edu.cn)

University of Jinan <https://orcid.org/0000-0002-5684-8954>

Research Article

Keywords: layered double hydroxide, nanocrystal morphology, persulfate, radical activation, catalytic degradation, organic pollutants

Posted Date: May 11th, 2022

DOI: <https://doi.org/10.21203/rs.3.rs-1535118/v1>

License:  This work is licensed under a Creative Commons Attribution 4.0 International License.

[Read Full License](#)

Abstract

Grasping how the morphology of a layered double hydroxide (LDH)-based catalyst alters its catalytic activity provides an available strategy for the rational design and fabrication of high-efficiency catalyst at micro-scale. Herein, three NiFe-LDH materials with different morphologies (2D-plate-like hexagon, 2D/3D-flower-like solid sphere and 2D/3D-flower-like hollow sphere) and regulable oxygen vacancies (OVs) were fabricated using a morphological regulation method of Ostwald ripening. The 2D/3D-flower-like hollow sphere NiFe-LDH (FH-NiFe-LDH) exhibited the most considerable activity for the abatement of acid orange 7 (AO7) with the first order rate constant up to $k = 0.023 \text{ min}^{-1}$. Characterizations demonstrated that FH-NiFe-LDH possessed a larger specific surface area, hence profoundly allowed for more exposure of active sites to facilitate electron transfer. Simultaneously, various concentrations of OVs were detected in the morphologically tunable NiFe-LDHs and enhanced the reactivity of OVs-connected Ni or Fe, therefore manifesting the morphologic origin of catalytic performance. According to the quenching experiments, sulfate radical ($\text{SO}_4^{\cdot-}$), hydroxyl radical ($\cdot\text{OH}$), and oxygen radical ($\text{O}_2^{\cdot-}$) were identified to be involved in the decomposition process.

1. Introduction

Catalysts with tunable morphology allow for controllable exposure of highly active atoms or regions, facilitate the capacity of electron transfer between substrates and catalysts, and hence profoundly favour the enhancement of catalytic activity. Comprehending the structural origin between morphology and activity provides an available strategy of chemical tailoring for active sites in inexpensive transition metal-based catalysts to enhance the catalytic activity (Li & Shen 2014, Strasser et al. 2018). Layered double hydroxides (LDH), as a typical representative of inorganic layered catalysts, has drawn much attention because of its unique supermolecule structure, controllable element composition, and diversified morphological architecture. Additionally, by virtue of the desirable properties, including low cost, high catalytic performance, durable stability, and unique structural properties (e.g., topological transitions, intercalation, and combination with other function materials), LDH-based catalysts have been extensively used in the fields of water splitting (Zubair et al. 2017), CO_2 reduction (Huang et al. 2019), photochemistry (Atienzar et al. 2011), and especially environmental remediation (Wang et al. 2018a). Designing (Fang et al. 2019, Hong et al. 2019, Wang et al. 2018b) micro-scale crystals of LDH with appropriate morphology can regulate their catalytic activity since the active center (e.g., defects, exposed facets, and electronic states, etc.) affected by tunable morphology can be trippingly handled for specific catalytic processes with improved activity. Recently, a series of LDH and their calcination products with various morphologies have been proposed as heterogeneous catalysts. For instance, NiFe-LDHs with flower-like, granular-sheet-like and sphere-like structures, etc., were successfully synthesized and exhibited different catalytic activity, reaffirming the morphological regulation of LDH can tailor the catalytic performance (Fang et al. 2019, Hong et al. 2019, Wang et al. 2018b). Therefore, rational design of LDH with tunable structure and morphology while satisfying the requirements simultaneously for the abatement of aqueous contaminants is a prospective micro-regulation strategy.

In decades, persulfate-based advanced oxidation processes (PS-AOPs) have received widespread academic advertence for the oxidation of aqueous refractory organics since these methods possess a strong oxidizing capability, high redox potential, and low energy input demands (Hodges et al. 2018, Ike et al. 2018). The mechanism of PS activation based on the radical-driven with reactive oxygen species (ROS) has been recognized by the majority of articles (Duan et al. 2018a, Duan et al. 2018b, Liu et al. 2019a, Zhang et al. 2014). To be specific, a typical PS activation process is as follows: Firstly, PS is adsorbed on the surface of the catalyst to form a complex; Secondly, electron transfer occurs from catalyst to PS; Thirdly, dissociation of the peroxide bonds (O-O) in $S_2O_8^{2-}$ groups of PS generates ROS (Duan et al. 2019, Li et al. 2016, Li et al. 2018b). To boost the production of ROS, the adsorption efficiency of PS molecules on the catalyst surface and the rates of electron transfer from catalyst to PS are considered to be an efficiency-determining step. Morphology-engineering not only provides a powerful approach to tailor the concentration of oxygen vacancies (OVs), strengthens the bonds between PS and catalyst, regulates the surface of active sites but also mediates electrochemical properties to facilitate the electron transfer, thus promoting the activation of PS (Liu et al. 2019b). Moreover, from the perspective of spatial structure, the structure of two-dimensional (2D) provides considerable specific area, leading to more active sites being exposed. The transfer path of electrons is also shortened by virtue of its thin thickness (Dong et al. 2020). Nevertheless, the structure of three-dimensional (3D) hierarchical can produce countless micro or nanopores that promote diffusion, transport, and adsorption for molecule units of contamination (Dong et al. 2020, Han et al. 2019). Consequently, constructing the novel 2D/3D homojunction with specific active sites via morphology-engineering is dramatically desired and significant to obtain the more high-efficiency and low-cost catalysts for further development of PS-AOPs.

To date, most of the reported studies merely obtained one kind of micro-structures for a specific goal. In addition, the comprehending of morphology engineering was superficial and mainly depended upon the serendipitous findings. Herein, inspired by the above contents, NiFe-LDH crystals with morphologies of 2D-plate-like hexagonal, 2D/3D-flower-like solid sphere, and 2D/3D-flower-like hollow sphere were synthesized and employed as model heterogeneous catalysts to activate PS for the decay of A07. A morphological regulation mechanism based on Ostwald ripening was applied to form hollow structures in which the F^- played a crucial role (Huang et al. 2017). The morphology-dependent catalytic performance was compared in detail. The results demonstrated that FH-NiFe-LDH revealed superior catalytic activity, with an apparent reaction rate constant at 0.023 min^{-1} , because of the existence of higher surface energy, higher OVs concentration, and excellent electrochemical properties. Simultaneously, the EPR analysis and quenching experiments proved that PS activation proceeded via a radical-driven procedure. In this case, OVs played a decisive role in accelerating electron transfer between catalysts and PS molecules in LDH/PS system. This study provides a valuable guideline for designing morphology-controlled LDH-based 2D/3D-homojunction to enhance the catalytic activity in the field of organic contaminants remediation.

2. Experimental Section

2.1 Materials and Chemicals

Nickel nitrate (98%), iron nitrate (97%), hydrochloric acid (38%), and tertiary butyl alcohol ($\geq 99.7\%$) were purchased from China National Medicines Corporation Ltd. (Beijing, China). Urea (99%), ammonium fluoride (NH_4F , 99.5%), ethanol ($\geq 99.7\%$), phenol ($\geq 99.0\%$), and p-benzoquinone ($\geq 98.0\%$), Sodium persulfate (98%), and acid orange 7 (AO7, 99%) were obtained from Macklin Ltd. (Shanghai, China). Deionized water was used in all experiments. All the chemicals were used without further purification.

2.2 Preparation of catalysts with different morphologies

2D/3D-flower-like hollow sphere NiFe-LDH (FH-NiFe-LDH) was prepared by the previous study with minor modifications (Huang et al. 2017). Ordinarily, 9 mmol $\text{Ni}(\text{NO}_3)_2 \cdot 6\text{H}_2\text{O}$, 3 mmol $\text{Fe}(\text{NO}_3)_3 \cdot 9\text{H}_2\text{O}$, 21 mmol urea, and 0.1g NH_4F were dissolved into 30mL methanol. Then the mixed solution was stirred continuously for 1 h. Next, the mixture was transferred into a Teflon-lined autoclave and kept at 140°C for 12 h. Lastly, the composites were gathered after washing with deionized water and ethanol three times, respectively. 2D/3D-flower-like solid sphere NiFe-LDH(FS-NiFe-LDH) was prepared by the similar synthetic method applied for FH-NiFe-LDH without NH_4F . 2D-plate-like hexagon NiFe-LDH(P-NiFe-LDH) was also prepared by the similar synthetic process used for FS-NiFe-LDH by deionized water instead of methanol.

2.3 Characterization of catalysts

Powder X-ray diffraction (XRD) date was collected from a Bruker D8 Advance X-ray diffractometer in reflection mode with a Cu-K α radiation source from 5° to 80°. SEM and TEM images were taken on a S4800 instrument (Hitachi Corporation, Germany) and a Talos F200S/FEI Tecnai G2 F20 X-Twin (FEI Company, USA). Fourier transform infrared (FT-IR) were examined by Nicolet 6700 spectrometer to analyze the chemical bonds. The specific surface area was measured by the nitrogen adsorption-adsorption isotherms at 77 K by nitrogen adsorption system (ASAP 2020, Micromeritics). X-ray photoelectron spectroscopy (XPS) spectra were recorded on Thermo Fisher, ESCALAB 250XI with Al-K α radiation (1486.6 eV) as X-ray source. The presence of oxygen vacancies was determined by Raman spectra (HORIBA Lab RAM HR Evolution) and Electron paramagnetic resonance (EPR) spectra (a Bruker A200 spectrometer at 9.432 GHz, using a 100-kHz field modulation frequency and a 1.0-G standard modulation amplitude). Electrochemical characterizations, including electrochemical impedance spectra (EIS) and cyclic voltammetry (CV) were measured through an electrochemical workstation (CHI608C). The concentrations of simulated AO7 solution was detected by high-performance liquid chromatography (HPLC, Agilent 1260 Infinity II) equipped with a C18 reversed phase column (4.6 × 250 mm) and a UV-DAD detector.

2.4 Evaluation of catalytic activity

The catalytic activity of the as-prepared catalysts was evaluated by activating PS for the abatement of AO7. Detailedly, 3 mg of catalysts homogeneity dispersed in 50 mL of 30 mg/L AO7 simulated wastewater. The adsorption–desorption equilibria was established after additional agitation in the dark for 30 min. The degradation reaction was triggered by the addition of appropriate PS solution. At regular

time intervals, 1 mL of the liquid sample was withdrawn by a syringe, rapidly filtered through a 0.22 μm filter, and then determined by the HPLC. For the durability test, the reacted catalysts were collected by centrifuged, washed with ethanol and deionized water, and then vacuum dried for further use.

3. Results And Discussion

3.1 Characterization analysis

To provide information for crystalline structure and phase composition of the as-synthesized catalysts in the presence of different morphologies, X-ray diffraction (XRD) was carried out. As illustrated in Fig. 1a, a series of peaks indexed as (003), (006), (012), and (110) located at 11.02°, 22.98°, 34.39°, and 59.26° were observed in all samples, which can be well-indexed to NiFe-LDH structure (*JCPDS card no. 40-0215*) (Miranda et al. 2014). Compared with the peaks of P-NiFe-LDH, the (003) reflection of FH-NiFe-LDH was shifted, while the (006) reflection was significantly shifted to lower angles, but the (110) reflection remained the same. This result may be attributed to lattice distortion reaction caused by residual stress, thus leading to more surface defects. Meanwhile, the peak width of FS-NiFe-LDH and FH-NiFe-LDH is significantly larger than P-NiFe-LDH, indicating that the crystal size in clusters is smaller. Through Bragg's equation, the intralayer spacing value of P-NiFe-LDH was calculated to be $\sim 7.72\text{\AA}$ from the (003) peak. However, the intralayer spacing value of FS-NiFe-LDH and FH-NiFe-LDH were calculated to be ~ 8.16 and $\sim 8.31\text{\AA}$, respectively. This data demonstrated that the interlayer spacing of the catalysts obviously increased, which was beneficial to pollutants' entering.

Figure 1b displays the FT-IR spectra of the as-prepared catalysts. The broad bands around the 3400–3600 cm^{-1} region are assigned to the -OH stretching vibrations of the surface-bound -OH group. The obvious -OH stretching vibration of P-NiFe-LDH may possess a superior affinity with water molecules to reveal strong hydrophilicity. A sharp absorption at $\sim 1375\text{ cm}^{-1}$ is observed in all samples, which ascribed to the asymmetric stretching type of CO_3^{2-} . Meanwhile, the peaks at ~ 795 , ~ 626 , and $\sim 432\text{ cm}^{-1}$ are assigned to M – O vibrations and M – O-H bending (M represent metals) (Li et al. 2008). Synchronously, two bands at ~ 2935 and $\sim 1051\text{ cm}^{-1}$ were watched in both FS-NiFe-LDH and FH-NiFe-LDH which were belonged to the bending vibration absorption of C – H and the C – O stretching of ethanol (Gao et al. 2014). The stretching vibration of the interlayer water is located at $\sim 1634\text{ cm}^{-1}$, while the carbonate in the layer of NiFe-LDH is observed by the strong band at 1385 cm^{-1} (Wang et al. 2015). The results further manifested the existence of intercalated -OH and CO_3^{2-} groups, as well as H_2O .

To further investigate the morphology and microstructure of the as-synthesized LDH, SEM was conducted (Fig. 2). A uniform morphology of plate-like hexagonal can be observed with an average lateral size 500 – 600 nm, while FH-NiFe-LDH and FS-NiFe-LDH composed of hierarchical flower-like spheres assembled by nanosheets with an average lateral size 800 – 900 nm. Simultaneously, the morphology of FS-NiFe-LDH and FH-NiFe-LDH is similar, except the latter is a spherical structure with a hollow inside. Moreover, both solid and hollow structures are obviously constructed by the unit of the hexagonal sheet, indicating that a

typical 2D/3D homojunction structure is successfully constructed. It has been reported that 2D/3D homojunction with natural matching chemical and electronic structures between structural units was more beneficial to transfer electrons at the interface (Liu et al. 2019b).

HR-TEM images of the as-prepared three catalysts with different morphologies were further analysed (Fig. 3). The images revealed the lattice fringe to be 0.334, 0.195, and 0.219 nm, which were consistent with (113), (112) and (115) planes of NiFe-LDH, respectively. Remarkably, the preferentially exposed {110} planes of FH-NiFe-LDH possess higher surface energy, which was verified by the reported theoretical calculation. Likewise, the HRTEM images also exhibited that FS-NiFe-LDH and FH-NiFe-LDH had mainly exposure of {110} facets. However, the {100} facets of P-NiFe-LDH are the exposed facets, which is well match with previous study (Zhang et al. 2021). Moreover, it was worth noticing that there were some voids in the overall morphology for FS-NiFe-LDH and FH-NiFe-LDH, indicating different amounts of defects on the surface of samples which more intuitively verifies the judgment on the location of different OVs defects.

To comprehend the origin of the catalytic activity, the specific surface and pore size distribution of the structures were explored by a N₂ adsorption/desorption analyzer. Figure 4a and b present the Brunauer-Emmett-Teller (BET) sorption isotherms and the corresponding distribution of Barrette-Joyner-Halenda (BJH) pore size. The pore size of NiFe-LDH was distributed in the mesoporous region, and specific surface areas (SSAs) decreased in the order FH-NiFe-LDH > FS-NiFe-LDH > P-NiFe-LDH, which corresponded to catalytic performance. This is because the increase of SSAs can accelerate mass transfer and maintain superior utilization efficiency of exposed active sites, thus enhancing catalytic performance (Liu et al. 2019b). Meanwhile, the isotherms exhibited hysteresis loops of varying intensities, which are consistent with the capillary condensation under high pressure. According to IUPAC classification, they could be categorized to the type IV with H3 type hysteresis loops (Song et al. 2015). The calculated BET specific surface area of the FH-NiFe-LDH was ~ 125.3487 m²·g⁻¹, higher than that of FS-NiFe-LDH (~ 74.7166 m²·g⁻¹) and P-NiFe-LDH (~ 60.1322 m²·g⁻¹). In addition, the total pore volumes of FS-NiFe-LDH and P-NiFe-LDH were ~ 0.2158 cm³·g⁻¹ and 0.0832 cm³·g⁻¹, respectively, while the total pore volume of FH-NiFe-LDH increased to ~ 0.3636 cm³·g⁻¹. The increase of pore volume might create more efficient transport routes to catalysts' internal voids and was conducive to the pollutant adsorption.

Considering the reactive facets can enrich abundant active sites, more exposed active facets are considered to be a decisive reason for improving catalytic performance. Generally, by virtue of the positive correlation between surface energy and chemical reactivity, the relatively less stable {110} facets theoretically exhibited higher reactivities than the stable {100} facet (Zhang et al. 2021). The conclusion proved that the catalytic activities of NiFe-LDH were primarily associated with the appearance of exposed facet which possessed high surface energies.

The surface chemical states and the elemental compositions of as-prepared catalysts were conducted by XPS (Fig. 5). The wide-scan high-resolution XPS spectra of the samples (Fig. 10a) demonstrate characteristic peaks of Ni 2p, Fe 2p, O 1s, and C 1s, indicating that there was no new element introduced

to the catalysts. As clearly revealed in Fig. 5a, the XPS spectrum of Ni 2p3/2 exhibited no apparent difference in three samples, indicating that the morphology did not change the chemical environment of Ni 2p. In comparation of the P-NiFe-LDH, the binding energy of Fe 2p 3/2 in FS-NiFe-LDH and FH-NiFe-LDH showed weak shift to lower region about 1.1 and 1.3 eV, respectively, evidencing that the Fe element in the latter accepted the electron. Correspondingly, a red-shifted was watched in both FS-NiFe-LDH and FH-NiFe-LDH by the spectra of O 1s, revealing that more electrons were transmitted (Wang et al. 2022). Hence, we speculated that crystal morphology-engineering could induce lattice distortion and thus resulting to the appearance of oxygen vacancies.

The XPS spectra of Ni 2p, Fe 2p, and O 1s were detailedly analyzed to further verify the above conclusion. Figure 6a displayed the XPS spectra of Ni 2p, the peaks centered at 853.1 and 855.2 eV were considered as Ni(\square) and Ni(\ominus), respectively (Liu et al. 2017, Wang et al. 2022). Another two peaks around 858.7 and 861.1 eV could be assigned to the satellite of Ni(\square) and Ni(\ominus), respectively. After calculation, the element proportions of the three catalysts were obtained. The proportion of Ni(\ominus) in FS-NiFe-LDH and FH-NiFe-LDH accounted for 40.12% and 41.07%, respectively, higher than P-NiFe-LDH (32.77%). As for the Fe element (Fig. 6b), the peaks centered at 708.5, 721.8, and 727.3 eV were corresponded to Fe(\square), another peak at 713.2 eV was attributed to Fe(\ominus) which coordinated to -OH (Wang et al. 2016). The proportion of Fe(\ominus) in P-NiFe-LDH accounted for 21.35%, while for the FS-NiFe-LDH and FH-NiFe-LDH samples, the proportion of Fe(\ominus) further increased to 38.84% and 38.16%, respectively, elucidating that the morphological change alters the surface electronic structure and leads to the conversion of valence state.

Due to a large number of localized electrons and surface suspended bonds, the OVs enable modulating the electronic states as well as the coordination structures of catalysts, thereby influencing its kinetics and catalytic performance (Sun et al. 2015). According to reported experimental and theoretical studies, the implantation of OVs may be beneficial to the adsorption and activation of PS molecules (Wu et al. 2020). Since morphology-engineering can regulate OVs concentration, we thoroughly believe that different morphology of NiFe-LDH crystals is expected to produce different concentrations of OVs, thus tuning their catalytic performance. Considering that the existence of OVs changes the coordination of the O atoms, the XPS of O 1s may be altered (Xu et al. 2021). Figure 6c exhibited the analysis of OVs species and concentrations by using O 1s spectrum. Three identified peaks at 529.5, 531.3, and 532.1 eV were adopted in the core-level spectra, respectively. In detail, two reflections at 530.8 and 532.1 eV were considered as surface lattice oxygen (O_L) and hydroxyl species (O_{OH}) (Zhuang et al. 2017), while another reflection at 531.3 eV could be corresponded to the formation of low oxygen coordination (Liu et al. 2016). The broad area of diverse integrated O_V reflection at 531.3 eV was found in FH-NiFe-LDH, demonstrating the maximum concentration of OVs. Remarkably, the integral-area ratios of O_V to ($O_L + O_{OH} + O_V$) were calculated to 0.3188, 0.3645 and 0.3878 for P-NiFe-LDH, FS-NiFe-LDH, and FH-NiFe-LDH, respectively. The $O_V / (O_L + O_{OH} + O_V)$ ratios decreased in the order FH-NiFe-LDH > FS-NiFe-LDH > P-NiFe-LDH, which was thoroughly in accordance with the tendency in catalytic performance. Obviously, the catalytic performance can be improved with the increase of OVs concentration. The catalytic activity was

positively correlated with OVs concentration, indicating that OVs was the active sites for the promotion of PS activation.

Figure 7a shows the Raman spectra of the three catalysts. In general, three peaks around positions 390, 420, and 460 cm⁻¹ were assigned to the symmetry of oxygen contact with metal ions in the octahedron (Devi & Srinivas 2017). The observed band around 685 cm⁻¹ was attributed to the symmetric stretching of Fe/Ni-O bond in tetrahedral coordination (Nandan et al. 2019). The intensity of the peaks may seem to be positively correlated with the amounts of cations in a vibrating substance that produce a signal peak. Moreover, a new band at around 528 cm⁻¹ appeared from OVs was found in the FH-NiFe-LDH, suggesting that the FH-NiFe-LDH possessed the superior concentration of OVs (Jia et al. 2017, Taniguchi et al. 2009).

To further elucidate that the differences in catalytic activity could be ascribed to the influences of OVs concentrations, EPR spectroscopy was used as a powerful tool to quantificationally analyse the existence and the concentration of OVs in different NiFe-LDH (Li et al. 2018a). As illustrated in Fig. 7b, the composites exhibited a strong symmetrical EPR signal at $g = 2.002$, which could be attributed to the paramagnetic OVs with 1 + charge state, agreeing with the previous study (Zhang et al. 2016). In addition, the signal intensity revealed that FH-NiFe-LDH possesses more OVs than the other two catalysts, also elucidated by the spectra of XPS. The EPR analysis would confirm that OVs were the active sites that primarily affected its electronic properties and facilitated bonding with PS molecules. It also contributed to the outstanding performance for FH-NiFe-LDH.

Electrochemical tests were conducted to verify the evaluate the electrical properties via morphology-engineering. The CV curves were illustrated in Fig. 8a, compared with other two catalysts, the FH-NiFe-LDH exhibited a larger area of window, evidencing larger capacitance, higher electric current density, and superior reducibility to coordinate a redox reaction. Meanwhile, two symmetrical reflections at -0.5 V and -0.42 V can be assigned to the redox couples of the valence conversion between Ni(II)/Ni(I) and Fe(II)/Fe(I). It was clear that the FH-NiFe-LDH exhibited the most promising peak current, evidencing that the highest catalytic activity. Furthermore, the EIS was also carried out, and Fig. 8b displayed the Nyquist plots of the catalysts. The FH-NiFe-LDH exhibited a relatively smaller electron transfer resistance, demonstrating superior conductivity and electron transfer capacity comparing with P-NiFe-LDH and FS-NiFe-LDH. Therefore, it was confirmed that the introduction of OVs by morphology-engineering could beneficial to enhance electrical conductivity, that is, accelerate the electron transfer between the catalyst and PS, hence dramatically facilitating the catalytic activity.

3.2. Catalytic performance

To investigate the effects of morphologies on NiFe-LDH catalytic activity, AO7 dye was selected as a model contaminant to compare the catalytic performance of the prepared catalysts (Fig. 9). All the degradation reactions were triggered at an initial pH of 6.80 at room temperature. Only PS was unreactive towards AO7, evidencing the radical generation by PS decomposition without catalyst dosage could be ignored under current conditions. We observed that AO7 removal by surface adsorption of the three catalysts is trivial (4.6%, 11.2%, 12.6%, respectively), demonstrating the major contribution of the catalytic

oxidation by PS decomposition. Nevertheless, because of the diverse morphology, especially the virtue of 3D structure, FH-NiFe-LDH and FS-NiFe-LDH exhibited superior adsorption performance compared to P-NiFe-LDH. It can be known the as-prepared three catalysts exhibited different catalytic activities. To better elucidate the catalytic activities, the first-order reaction kinetic model was employed to calculate the apparent rate constant for AO7 degradation. The apparent reaction rate constant (k) was 0.023 min^{-1} for FH-NiFe-LDH, while 0.01116 min^{-1} and 0.00631 min^{-1} for FS-NiFe-LDH and P-NiFe-LDH, respectively. The above results show that the catalytic activity for LDH catalysts is in the order of FH-NiFe-LDH > FS-NiFe-LDH > P-NiFe-LDH, indicating that the porous FH-NiFe-LDH with more OVs modification has higher catalytic activity. Moreover, the rate constant for FH-NiFe-LDH was approximately 3 times higher than that of P-NiFe-LDH, emphasizing the decisive impact of morphology on the catalytic activities. The conclusions further highlighted that morphology engineering could tailor the catalytic activity of NiFe-LDH.

3.3. Reusability and stability potential of catalyst

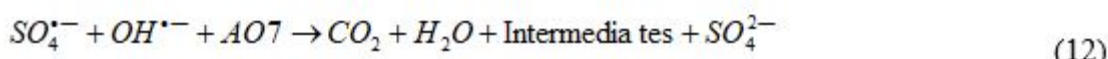
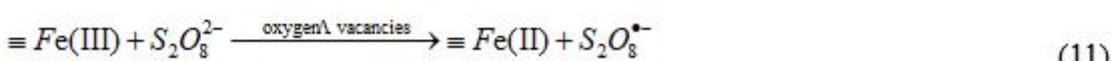
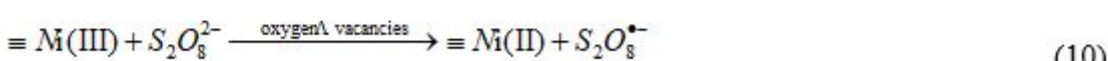
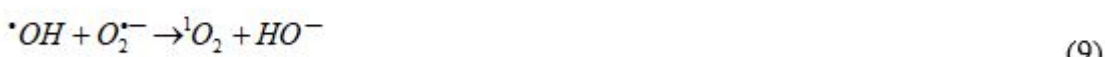
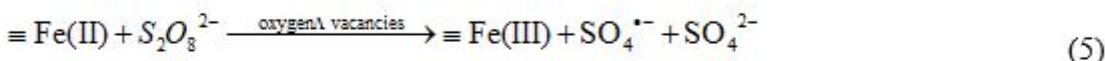
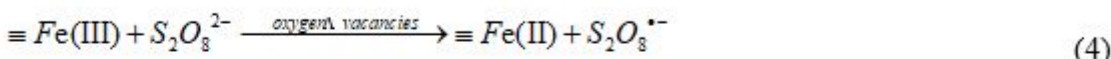
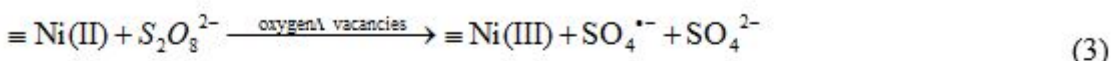
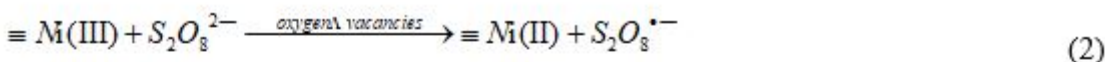
The durability of catalyst plays a vital role in catalytic degradation process via PS activation. Repetitive trials were performed to grasp detailed information of the catalytic performance for AO7 degradation. As exhibited in Fig. 10, the AO7 degradation efficiency can maintain a slight change within 240 min after consecutive 3 cycles, manifesting the prominent stability of catalysts. The minor decrease of catalytic performance during the repetitive tests could be attributed to the aggregation and blockage of the catalyst, resulting the decrease of surface catalytic active sites and hence inhibiting the reaction between catalyst and oxidant. Moreover, as revealed in XPS analysis, the elemental compositions are maintained well after reaction, further evidencing respectable robustness of the NiFe-LDH for AO7 degradation via PS activation. In conclusion, the NiFe-LDH possess the outstanding activity and respectable stability and exhibit a promising advantage for environmental remediation.

3.4. Identification of reactive species and possible activation mechanisms

The conversion of Ni(II)/Ni(III) and Fe(II)/Fe(III) occurs during the active catalytic process on the LDH surface. To further explore the mechanism of catalytic active sites involved in the degradation differences among the catalysts, the XPS analysis was applied on the reacted NiFe-LDH. As illustrated the Ni 2p spectra in Fig. 11a and 11b, after the catalytic reaction, the Ni(II) and Fe(II) content of NiFe-LDH accounted for 41.07% and 38.16%, respectively, before the catalytic reaction, while the Ni(III) and Fe(III) content were converted to 35.86% and 26.95%, respectively, after the catalytic reaction, signifying Ni(II)/Ni(III) and Fe(II)/Fe(III) redox reaction process was contained for PS activation. Simultaneously, as displayed in O 1s spectra (Fig. 12c), the relative concentration of OVs decreased after the reaction (20.97% vs 38.78% of the fresh one), evidencing that the OVs in the NiFe-LDH involved in the activation of PS. Of note, the concentration of surface OVs species on the reacted NiFe-LDH can be still maintain a better level.

To uncover the reaction mechanism in the LDH/PS system with different morphologies, radical quenching experiment was performed to investigate the involved reactive species. It is widely recognized that active radicals including $\cdot\text{OH}$, $\text{SO}_4^{\cdot-}$, and $\text{O}_2^{\cdot-}$ are produced in the process of PS activation. Herein, the frequently-used radical scavengers (EtOH and TBA) were chosen to differentiate the contribution of $\text{SO}_4^{\cdot-}$ and $\cdot\text{OH}$, while p-BQ was used as the scavengers for $\text{O}_2^{\cdot-}$. Phenol was used to validate surface-bonded radicals due to its weak polarity and the ability to consume $\text{SO}_4^{\cdot-}$ and $\text{O}_2^{\cdot-}$ when approach the solid–liquid interface (Wu et al. 2020). As shown in Fig. 12, the removal efficiency of A07 was 36.2%, 50.1% and 79.8% without adding any scavenger in the presence of P-LDH, FS-LDH, and FH-LDH, respectively. For the P-LDH/PS system (Fig. 12a), the degradation rate of A07 decrease to 22.5% and 10.5% in the presence of TBA and EtOH, respectively, manifesting that the existence of both $\cdot\text{OH}$ and $\text{SO}_4^{\cdot-}$, and notably, $\text{SO}_4^{\cdot-}$ was more efficient for A07 removal than $\cdot\text{OH}$. Moreover, in the presence of p-BQ, the decay of A07 declined to ~ 26.8%, demonstrating that $\text{O}_2^{\cdot-}$ was also involved in A07 degradation. Similar phenomena were also observed for FS-LDH/PS and FH-LDH/PS system (Fig. 12b and 12c) in the presence of TBA and EtOH. However, as clearly observed, the inhibitory effect of p-BQ was significantly enhanced in FS-LDH/PS and FH-LDH/PS system, indicating that $\text{O}_2^{\cdot-}$ play a dominant role. The experimental results further confirmed that tailoring the morphology of LDH could result in different OVs concentrations. Moreover, the removal efficiency of A07 decreased to 9.5%, 18.2 and 20.5% in the presence of phenol, demonstrating that the reactive species could be originally generated on the surface of LDH and then some of it would diffuse into the liquid phase in LDH/PS system. In summary, three kinds of ROS including $\cdot\text{OH}$, $\text{SO}_4^{\cdot-}$, and $\text{O}_2^{\cdot-}$ corporately contribute to the A07 elimination in LDH/PS system, and the degradation reaction belongs to surface reaction.

Based on the above detailed analysis, we systematically proposed the overall mechanism of PS activation in LDH/PS system (Fig. 13). In brief, PS molecules diffuse to the surface of NiFe-LDH and adsorb on the surface-active site of catalyst. Then, PS molecules are activated via electron transfer and produce a series of ROS to attack the contaminant. It is worth noting that because of the abundant diffusion pathway combined with nano-confinement and nano-enrichment, the unique hollow structure with 2D/3D homojunction in FH-NiFe-LDH can deeply boost surface adsorption and the mass diffusion. Meanwhile, with the existence of OVs in FH-NiFe-LDH, the efficiency of electron transfer to PS can be facilitated, thus enhancing PS activation.



According to aforementioned analysis in association with the reported accounts (Bu et al. 2021, Guo et al. 2020, Wu et al. 2020), the PS activation and ROS generation mechanism can be detailedly displayed in Eqs. (1)-(12). Expressly, the PS molecule firstly accepts an electron from Ni(II) or Fe(II) on the surface of NiFe-LDH to produce $SO_4^{\cdot-}$. The redox cycle could accomplish via the reaction between Ni(III)/Fe(III) and $S_2O_8^{2-}$ for consecutive production of $SO_4^{\cdot-}$. Then, $SO_4^{\cdot-}$ could further convert H_2O to $\cdot OH$. (Eqs. (6)– (8)). Notably, the OVs also play a vital role in facilitating the production of more active sites for PS activation. Impressively, NiFe-LDH featuring abundant OVs could react with O_2 to generate $O_2^{\cdot-}$ (Eq. (1)). During this process, OVs could accelerate the electron transfer to promote the generation of ROS, meanwhile, facilitate the redox cycle of Fe(III)/Fe(II) and Ni(III)/Ni(II) (Wang et al. 2022). Finally, the active radicals attacked the AO7 and quickly eliminated AO7.

4. Conclusions

In summary, a class of NiFe-LDH catalysts with 2D-plate-like hexagonal, 2D/3D-flower-like solid sphere, and 2D/3D-flower-like hollow sphere morphologies is evidenced for dramatically improved catalytic activities for pollution treatment by PS activation. The unique morphological structure regarding 2D/3D homojunction hollow spheres with extended interior space enables ensuring more exposure of the active

sites and providing efficient mass diffusion. Encouragingly, the characterization unravels that the morphology-engineering by OVs incorporation can skillfully regulate the surface electronic state and local coordination environment, leading to stronger binding energy and accelerating charge transfer for enhanced PS activation. The different concentrations of OVs ascribed to the synergistic contribution of textural structures, exposed reactive facets, and aggregate size. Combined with the EPR and quenching experiments, the ROS in the LDH/PS system was identified to be $\text{SO}_4^{\cdot-}$, $\cdot\text{OH}$, and $\text{O}_2^{\cdot-}$, which account for the degradation of A07. We also predict that these results are not unique to NiFe-LDH, and that other transition metal hydroxide or oxide in which OVs can reveal the same catalytic processes. This study provides a fundamental comprehending of catalytic activities in morphologically tunable LDH and also inspire practical approaches for the rational design of morphology-controlled, high-efficiency catalysts.

Declarations

5.1 Ethics approval and consent to participate

Not applicable.

5.2 Consent for publication

Not applicable.

5.3 Availability of data and materials

All data generated or analysed during this study are included in this published article.

5.4 Competing interests

The authors declare that they have no competing interests.

5.5 Funding

This work was financially supported by the National Natural Science Foundation of China (Grant Nos. 41877132 and 51908242), Shandong Provincial Natural Science Foundation of China (Grant No. ZR2020KB009), and Science and Technology Program of University of Jinan (Grant No. XKY1918).

5.6 Authors' contributions

Rongyao Wang analyzed and interpreted the data and was a major contributor in writing the manuscript. Yanjun Yu performed formal analysis, writing-review & editing and supervision. Ruijuan Zhang performed investigation and formal analysis. Xiaohua Ren performed visualization, supervision, validation and formal analysis. Weilin Guo performed supervision, conceptualization, resources, writing-reviewing and editing, project administration and funding acquisition. All authors read and approved the final manuscript.

5.7 Acknowledgements

This work was financially supported by the National Natural Science Foundation of China (Grant Nos. 41877132 and 51908242), Shandong Provincial Natural Science Foundation of China (Grant No. ZR2020KB009), and Science and Technology Program of University of Jinan (Grant No. XKY1918).

References

1. Atienzar P, de Victoria-Rodriguez M, Juanes O, Rodríguez-Ubis JC, Brunet E, García HJE, *Science* E (2011) Layered γ -zirconium phosphate as novel semiconductor for dye sensitized solar cells: Improvement of photovoltaic efficiency by intercalation of a ruthenium complex-viologen dyad. 4:4718–4726
2. Bu Y, Li H, Yu W, Pan Y, Li L, Wang Y, Pu L, Ding J, Gao G, Pan BJES, *Technology* (2021) Peroxydisulfate activation and singlet oxygen generation by oxygen vacancy for degradation of contaminants. 55:2110–2120
3. Devi LG, Srinivas MJJoece (2017) Hydrothermal synthesis of reduced graphene oxide-CoFe2O4 heteroarchitecture for high visible light photocatalytic activity: Exploration of efficiency, stability and mechanistic pathways. 5:3243–3255
4. Dong H, Zhang X, Li J, Zhou P, Yu S, Song N, Liu C, Che G, Li CJACBE (2020) Construction of morphology-controlled nonmetal 2D/3D homojunction towards enhancing photocatalytic activity and mechanism insight. 263:118270
5. Duan X, Sun H, Shao Z, Wang SJACBE (2018a) : Nonradical reactions in environmental remediation processes: uncertainty and challenges. 224, 973–982
6. Duan X, Sun H, Wang SJAoCR (2018b) Metal-free carbocatalysis in advanced oxidation reactions. 51:678–687
7. Duan X, Kang J, Tian W, Zhang H, Ho S-H, Zhu Y-A, Ao Z, Sun H, Wang SJACBE (2019) Interfacial-engineered cobalt@ carbon hybrids for synergistically boosted evolution of sulfate radicals toward green oxidation. 256:117795
8. Fang P, Wang Z, Wang WJC (2019) Enhanced photocatalytic performance of ZnTi-LDHs with morphology control. 21:7025–7031
9. Gao C, Yu X-Y, Luo T, Jia Y, Sun B, Liu J-H, Huang X-JJJomCA (2014) Millimeter-sized Mg-Al-LDH nanoflake impregnated magnetic alginate beads (LDH-n-MABs): a novel bio-based sorbent for the removal of fluoride in water. 2:2119–2128
10. Guo XX, Hu TT, Meng B, Sun Y, Han Y-FJACBE (2020) Catalytic degradation of anthraquinones-containing H₂O₂ production effluent over layered Co-Cu hydroxides: defects facilitating hydroxyl radicals generation. 260:118157
11. Han X, Yuan A, Yao C, Xi F, Liu J, Dong XJJomMS (2019) Synergistic effects of phosphorous/sulfur co-doping and morphological regulation for enhanced photocatalytic performance of graphitic carbon nitride nanosheets. 54:1593–1605

12. Hodges BC, Cates EL, Kim J-HJNn (2018) : Challenges and prospects of advanced oxidation water treatment processes using catalytic nanomaterials. 13, 642–650
13. Hong Y, Peng J, Zhao X, Yan Y, Lai B, Yao GJCEJ (2019) Efficient degradation of atrazine by CoMgAl layered double oxides catalyzed peroxymonosulfate: optimization, degradation pathways and mechanism. 370:354–363
14. Huang L, Zou Y, Chen D, Wang SJCJoC (2019) Electronic structure regulation on layered double hydroxides for oxygen evolution reaction. 40:1822–1840
15. Huang P, Liu J, Wei F, Zhu Y, Wang X, Cao C, Song WJMCF (2017) Size-selective adsorption of anionic dyes induced by the layer space in layered double hydroxide hollow microspheres. 1:1550–1555
16. Ike IA, Linden KG, Orbell JD, Duke MJCEJ (2018) : Critical review of the science and sustainability of persulphate advanced oxidation processes. 338, 651–669
17. Jia J, Yang W, Zhang P, Zhang JJACAG (2017) Facile synthesis of Fe-modified manganese oxide with high content of oxygen vacancies for efficient airborne ozone destruction. 546:79–86
18. Li J-J, Weng B, Cai S-C, Chen J, Jia H-P, Xu Y-JJJohm (2018a) Efficient promotion of charge transfer and separation in hydrogenated TiO₂/WO₃ with rich surface-oxygen-vacancies for photodecomposition of gaseous toluene. 342:661–669
19. Li M, Chen S, Ni F, Wang Y, Wang LJEa (2008) Layered double hydroxides functionalized with anionic surfactant: Direct electrochemistry and electrocatalysis of hemoglobin. 53:7255–7260
20. Li X, Ao Z, Liu J, Sun H, Rykov Al, Wang JJAn (2016) Topotactic transformation of metal–organic frameworks to graphene-encapsulated transition-metal nitrides as efficient Fenton-like catalysts. 10:11532–11540
21. Li X, Huang X, Xi S, Miao S, Ding J, Cai W, Liu S, Yang X, Yang H, Gao JJotACS (2018b) Single cobalt atoms anchored on porous N-doped graphene with dual reaction sites for efficient Fenton-like catalysis. 140:12469–12475
22. Li Y, Shen W (2014) Morphology-dependent nanocatalysts: rod-shaped oxides. Chem Soc Rev 43:1543–1574
23. Liu H, Wang Y, Lu X, Hu Y, Zhu G, Chen R, Ma L, Zhu H, Tie Z, Liu JJNE (2017) The effects of Al substitution and partial dissolution on ultrathin NiFeAl trinary layered double hydroxide nanosheets for oxygen evolution reaction in alkaline solution. 35:350–357
24. Liu L, Liu Q, Wang Y, Huang J, Wang W, Duan L, Yang X, Yu X, Han X, Liu NJACBE (2019a) Nonradical activation of peroxydisulfate promoted by oxygen vacancy-laden NiO for catalytic phenol oxidative polymerization. 254:166–173
25. Liu L, Wang Y, Liu Q, Wang W, Duan L, Yang X, Yi S, Xue X, Zhang JJACBE (2019b) Activating peroxydisulfate by morphology-dependent NiO catalysts: Structural origin of different catalytic properties. 256:117806
26. Liu PF, Yang S, Zhang B, Yang, HGJAam (2016) interfaces : Defect-rich ultrathin cobalt–iron layered double hydroxide for electrochemical overall water splitting. 8, 34474–34481

27. Miranda LD, Bellato CR, Fontes MP de Almeida MF, Milagres JL, Minim LAJCEJ (2014) Preparation and evaluation of hydrotalcite-iron oxide magnetic organocomposite intercalated with surfactants for cationic methylene blue dye removal. 254:88–97
28. Nandan B, Bhatnagar M, Kashyap SCJJJoP (2019) Cation distribution in nanocrystalline cobalt substituted nickel ferrites: X-ray diffraction and Raman spectroscopic investigations. 129:298–306Solids Co
29. Song H, Zhang C, Liu Y, Liu C, Nan X, Cao GJJJoPS (2015) Facile synthesis of mesoporous V2O5 nanosheets with superior rate capability and excellent cycling stability for lithium ion batteries. 294:1–7
30. Strasser P, Gliech M, Kuehl S, Moeller TJCSR (2018) Electrochemical processes on solid shaped nanoparticles with defined facets. 47:715–735
31. Sun Y, Gao S, Lei F, Xie YJCSR (2015) Atomically-thin two-dimensional sheets for understanding active sites in catalysis. 44:623–636
32. Taniguchi T, Watanabe T, Sugiyama N, Subramani A, Wagata H, Matsushita N, Yoshimura MJTJoPCC (2009) Identifying defects in ceria-based nanocrystals by UV resonance Raman spectroscopy. 113:19789–19793
33. Wang Q, Chen L, Guan S, Zhang X, Wang B, Cao X, Yu Z, He Y, Evans DG, Feng JJAC (2018a) Ultrathin and vacancy-rich CoAl-layered double hydroxide/graphite oxide catalysts: promotional effect of cobalt vacancies and oxygen vacancies in alcohol oxidation. 8:3104–3115
34. Wang Q, Wang X, Tian BJWS, Technology (2018b) Catalytic performances of Ni/Fe layered double hydroxides fabricated via different methods in Fenton-like processes. 77:2772–2780
35. Wang R, Yu Y, Zhang R, Ren X, Guo WJS, Technology P (2022) Vacancy-rich structure inducing efficient persulfate activation for tetracycline degradation over Ni-Fe layered double hydroxide nanosheets. 289:120663
36. Wang X, Spörer Y, Leuteritz A, Kuehnert I, Wagenknecht U, Heinrich G, Wang D-YJRa (2015) Comparative study of the synergistic effect of binary and ternary LDH with intumescence flame retardant on the properties of polypropylene composites. 5:78979–78985
37. Wang Y, Liu D, Liu Z, Xie C, Huo J, Wang SJCC (2016) Porous cobalt–iron nitride nanowires as excellent bifunctional electrocatalysts for overall water splitting. 52:12614–12617
38. Wu L, Hong J, Zhang Q, Chen B-Y, Wang J, Dong ZJCEJ (2020) Deciphering highly resistant characteristics to different pHs of oxygen vacancy-rich Fe₂Co₁-LDH/PS system for bisphenol A degradation. 385:123620
39. Xu W, Xue W, Huang H, Wang J, Zhong C, Mei DJACBE (2021) Morphology controlled synthesis of α-Fe₂O₃-x with benzimidazole-modified Fe-MOFs for enhanced photo-Fenton-like catalysis. 291:120129
40. Zhang N, Li X, Ye H, Chen S, Ju H, Liu D, Lin Y, Ye W, Wang C, Xu QJJotACS (2016) Oxide defect engineering enables to couple solar energy into oxygen activation. 138:8928–8935

41. Zhang T, Chen Y, Wang Y, Le Roux J, Yang Y, Croue J-PJEs, technology (2014) Efficient peroxydisulfate activation process not relying on sulfate radical generation for water pollutant degradation. 48:5868–5875
 42. Zhang Y, Xie W, Ma J, Chen L, Chen C, Zhang X, Shao MJJoEC (2021) Active facet determination of layered double hydroxide for oxygen evolution reaction. 60:127–134
 43. Zhuang L, Ge L, Yang Y, Li M, Jia Y, Yao X, Zhu ZJAM (2017) Ultrathin iron-cobalt oxide nanosheets with abundant oxygen vacancies for the oxygen evolution reaction. 29:1606793
 44. Zubair M, Daud M, McKay G, Shehzad F, Al-Harthi MAJACS (2017) Recent progress in layered double hydroxides (LDH)-containing hybrids as adsorbents for water remediation. 143:279–292

Figures

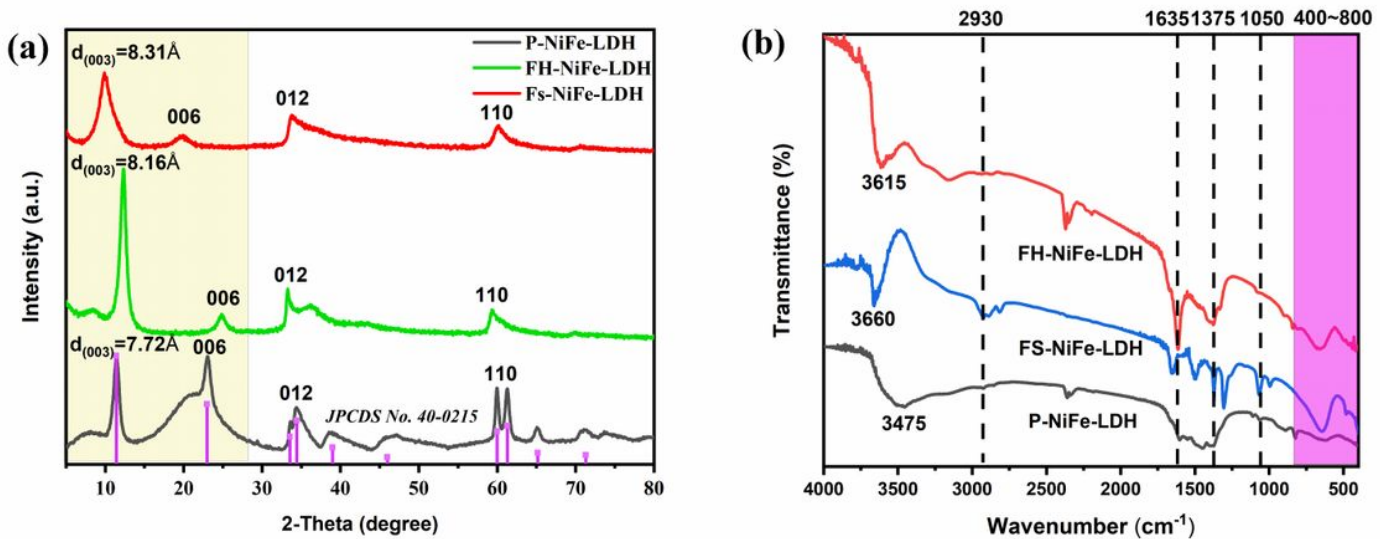


Figure 1

XRD patterns (a) and FT-IR spectra (b) of P-NiFe-LDH, FS-NiFe-LDH, and FH-NiFe-LDH.

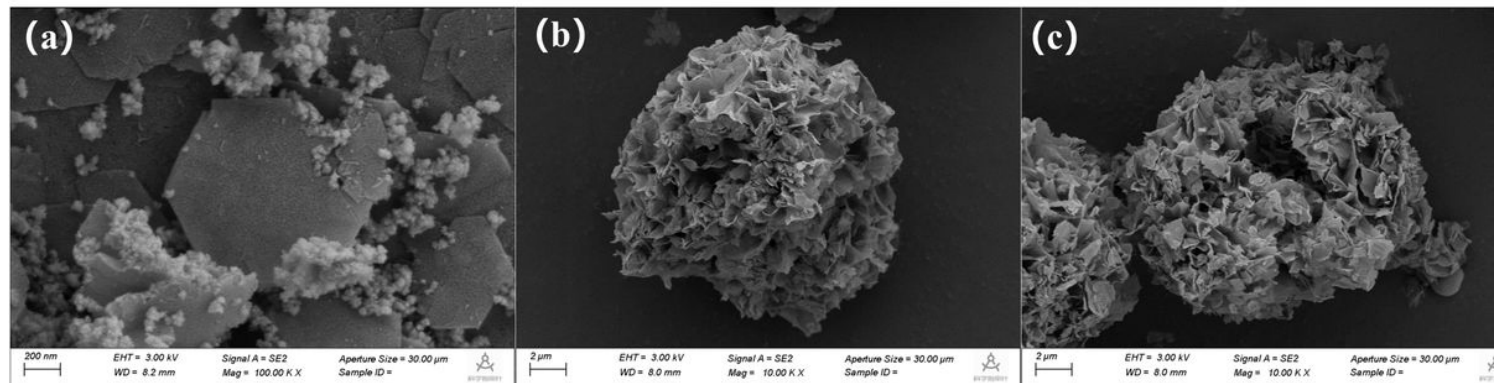


Figure 2

SEM images of (a) P-NiFe-LDH, (b) FS-NiFe-LDH, and (c) FH-NiFe-LDH.

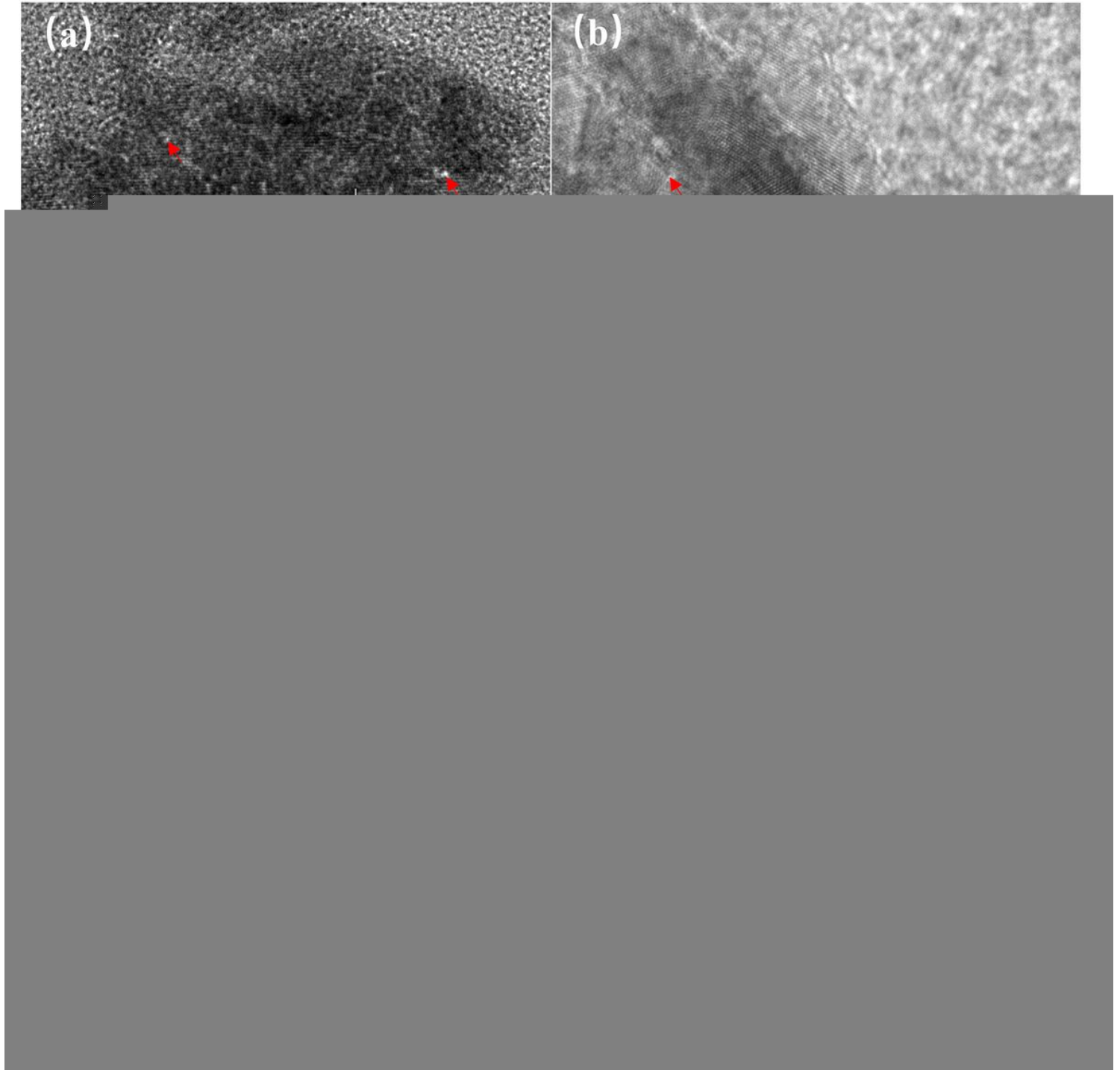


Figure 3

High-resolution TEM images of (a) P-NiFe-LDH, (b) FS-NiFe-LDH, and (c) FH-NiFe-LDH.

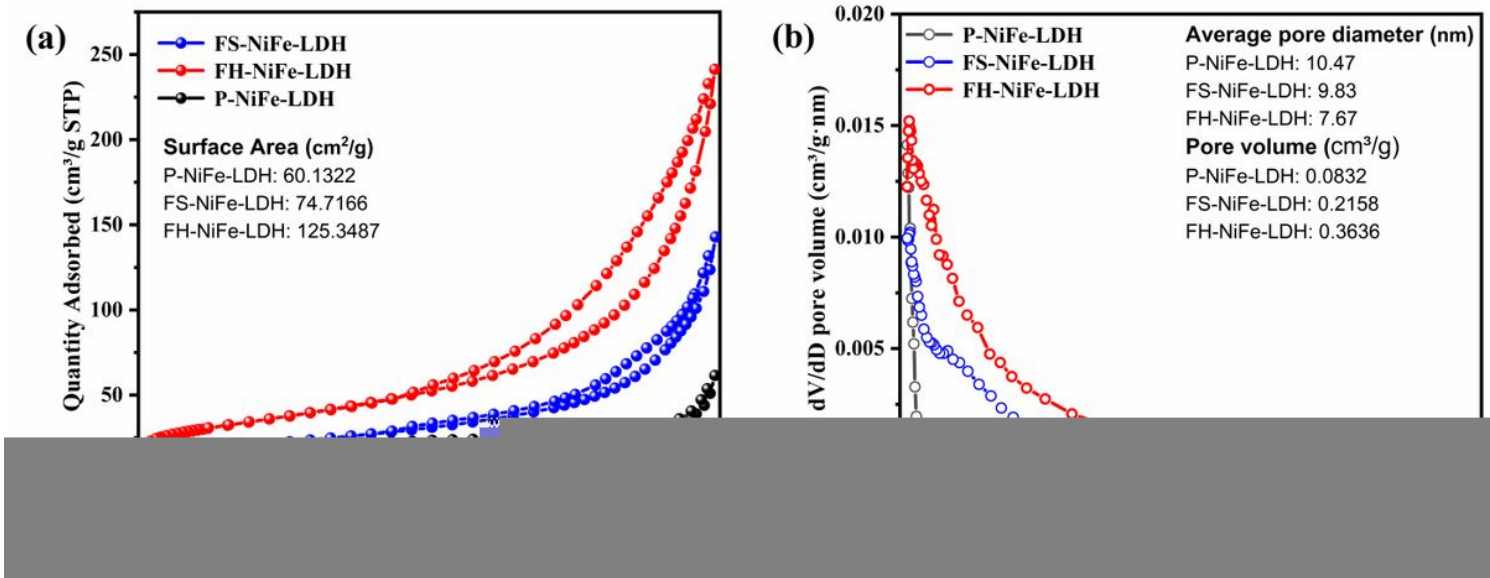


Figure 4

(a) Nitrogen(N_2) adsorption/desorption isotherm and (b) the corresponding BJH pore-size distribution curves of P-NiFe-LDH, FS-NiFe-LDH, and FH-NiFe-LDH.

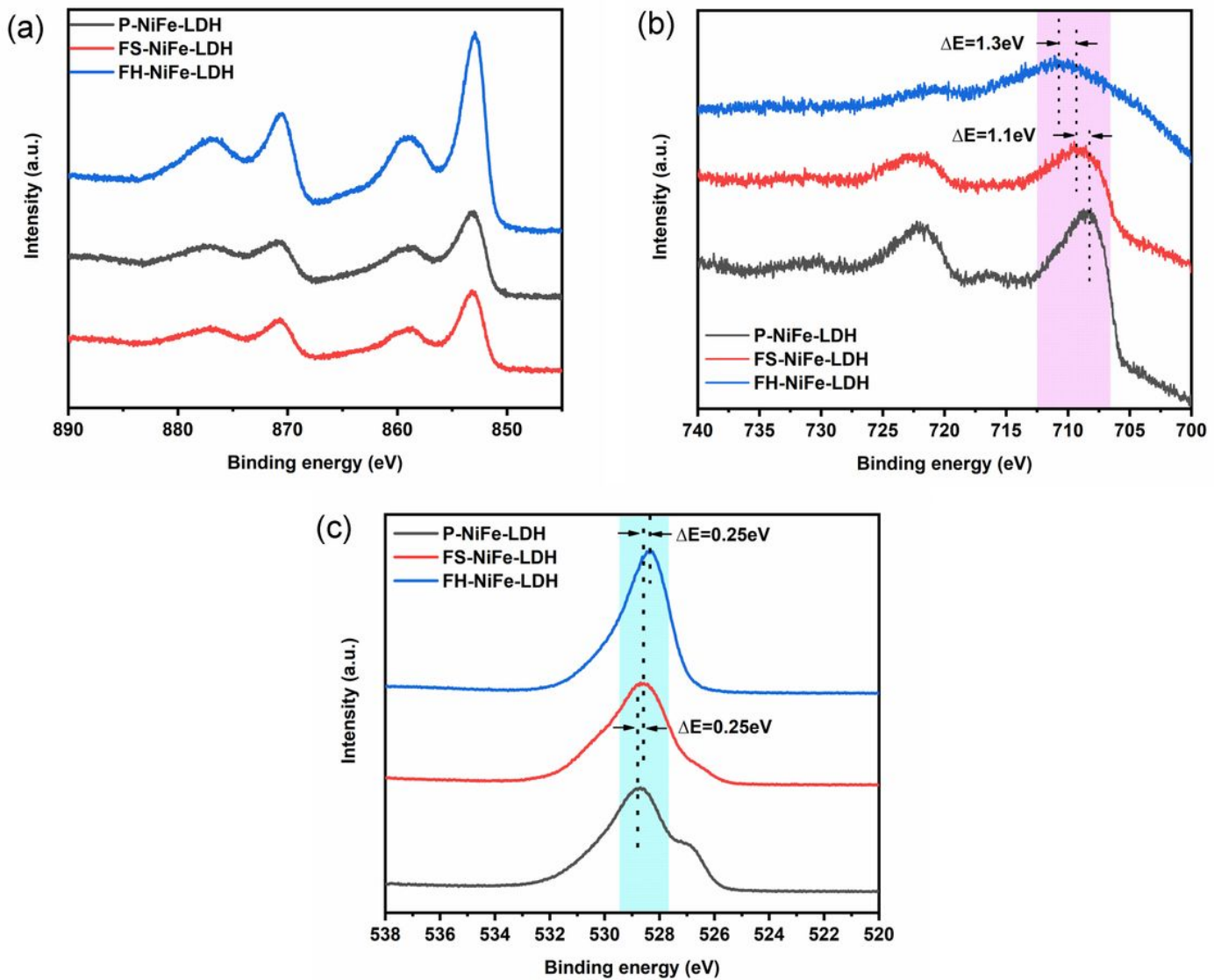


Figure 5

High resolution XPS spectra of Ni 2p, Fe 2p, and O 1s for P-NiFe-LDH, FS-NiFe-LDH and FH-NiFe-LDH.

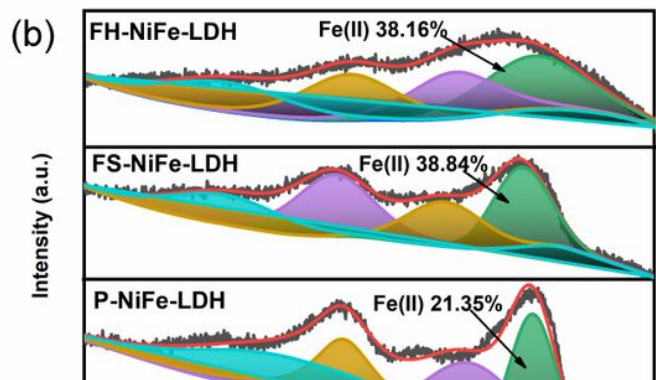
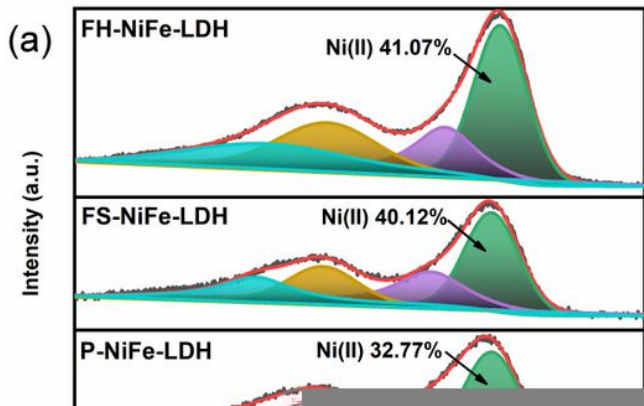


Figure 6

The XPS spectra of Fe 2p (a), Ni 2p (b) and O 1s (c) for the catalysts.

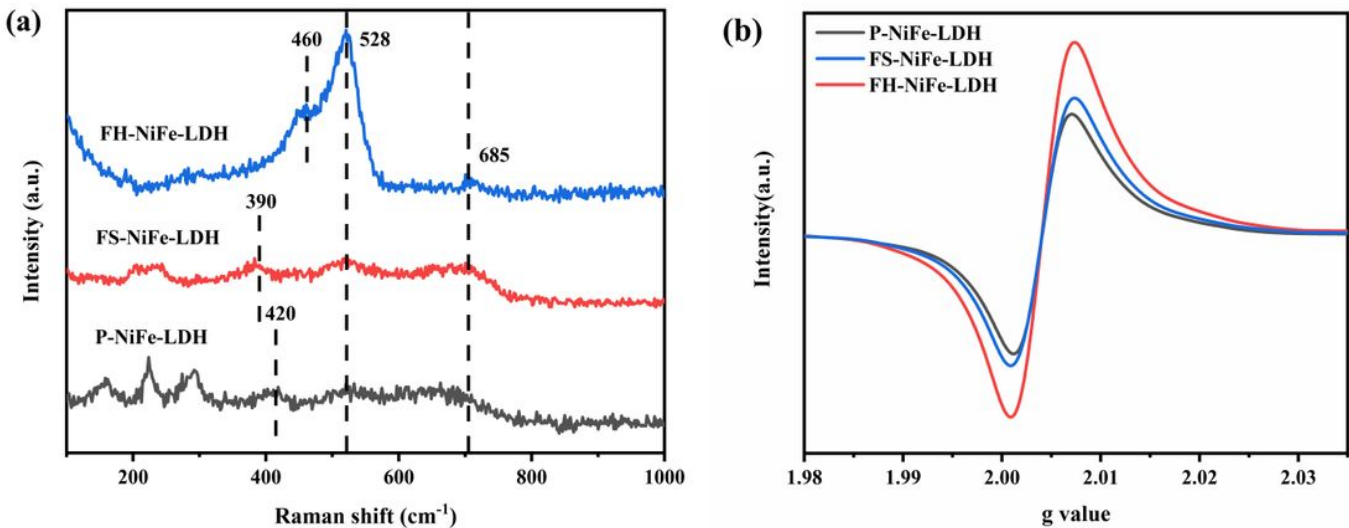


Figure 7

Raman (a) and EPR (b) spectra of P-NiFe-LDH, FS-NiFe-LDH and FH-NiFe-LDH.

Figure 8

(a) CV curves, and (c) EIS Nyquist plots of the catalysts.

Figure 9

The degradation efficiency of A07 in different reaction system.

Figure 10

The XPS spectra before and after reaction (a) and the reusability of the NiFe-LDH for A07 degradation (b).

Figure 11

XPS spectra for Ni 2p (a), Fe 2p (b), and O 1s (c) regions of catalysts before and after the reaction.

Figure 12

Effects of EtOH, TBA, and p-BQ on AO7 removal; (a) P-LDH; (b) FS-LDH;(c) FH-LDH.

Figure 13

Schematic diagram illustration of the reaction mechanism for the catalytic degradation of AO7 by morphology-controlled NiFe-LDH.